Multiphysics Reliability Simulation and Validation of a Flip-Chip Build-Up Film Crack via Piezoresistive Stress Sensor

Yutaka Suzuki[1], Jaimal Williamson[1], Blake Travis1, Tobias Fritz[2], Cynthia Chapa[3], Rajen Murugan[1]
[1,3]Texas Instruments, Inc.
12500 TI Boulevard
Dallas, Texas, 75243, U.S.A
[2]Texas Instruments Deutschland GmbH, Haggertystraße.
1, D-85356 Freising

[1]Worldwide Semiconductor Packaging
[2]WPRAMPS R&D HC FREI
[3]Worldwide Quality and Reliability Engineering
Email: y-suzuki@ti.com

Abstract

Flip-chip (FC) packaging technology in semiconductors has revolutionized the industry with high-performance and cost-effective solutions. However, aggressive miniaturization and integration are making mechanical reliability challenges more prevalent. Build-up passivation film crack due to interfacial delamination is becoming a growing reliability challenge. In this work, an innovative coupled multiphysics (thermomechanical) predictive modeling methodology is developed to quantify the localized structural stress magnitude and distribution under realistic thermal cycling. The predictive method employs finite element analysis (FEA) and digital image correlation (DIC) techniques to model the local thermal strain due to different coefficients of thermal expansion (CTE) at the metal and dielectric interface. The homogenization model adopting an image processing technique based on the light intensity analysis (LIA) was also developed to reflect the regional copper trace in the substrate with a broader range. The novelty of the current approach is the inclusion of DIC to accurately capture the localized strain in the region of interest under realistic thermal transient switching conditions. The dynamic mechanical analysis (DMA) technique characterized the rate-dependent mechanical properties. For the correlation phase to find critical parameters, 42 (6x7 array) piezoresistive stress sensors were implemented on the test chips design to ensure accurate and repeatable direct measurement of the stress distribution. This piezoresistive stress sensor was calibrated by a 4-point bending test that resulted in constant uniaxial stress at a fixed load, which was conducted by applying mechanical bending and controlling the stress sweep from compressive to tensile. Critical findings for achieving good correlations of stress distribution and magnitude between the multiphysics simulation flow results and measured data are utilizing rate-dependent properties and reflecting manufacturing process parameters. Generally, the FEA-based thermo-mechanical model under the reliability test loading is performed to evaluate the reliability performance and find the root causes. However, a multiphysics simulation approach and flow reflect that the temperature gradients have the potential to induce more significant stress concentrations based on the thermal simulation, which cannot be captured by using the typical conventional methodology. This methodology can be utilized to mitigate unexpected failure risks for future devices at the design stage. The predictive method developed here can be employed to predict thermomechanical reliability early in the semiconductor device design process.

Key words

Flip-Chip Package, Piezoresistive stress sensor, DIC, Modeling, Multiphysics, Thermomechanical.

I. Introduction

With the increasing adoption of Flip Chip (FC) packaging technology in various applications, the mechanical reliability challenges are becoming more pronounced. Interfacial delamination, crack, and excessive warpage are common issues encountered during reliability tests. The build-up passivation crack observed under the temperature cycle (TC) test is a typical failure mode (figure. 1). This crack is a result of the local coefficient of thermal expansion (CTE) mismatch of the interface between the different materials. Understanding these interfacial mechanical properties is crucial in identifying the root causes of failure modes. While thermo-mechanical analysis (TMA) is widely used to obtain the coefficient of thermal expansion (CTE), it falls short of accurately capturing the thermal strain at the local region. A digital-image correlation (DIC) was developed to estimate the thermal strain in the local region utilizing optical methodology with binocular vision extracting the x-y plane coordinate and the z directional coordinate, which can compute the thermal strain in the x-y plane. This study leveraged DIC and FEA coupled with computational fluid dynamics (CFD) thermal modeling to estimate the localized thermal strain precisely. Furthermore, assessing the exact stress magnitude is challenging due to its complex structure, the bill of material (BOM) set, and process flow for the semiconductor devices. A piezoresistive stress sensor is the best solution for clarifying the aforementioned features. These piezoresistive stress sensors should be calibrated before assembly to reflect any residual stress via the manufacturing process of semiconductor devices to correlate with FEA. Another concern would be stress increments based on the instantaneous temperature rises at the local hotspot regions. The evaluation of rate-dependent properties, known as viscoelasticity, should also be conducted to reflect the stress factors.

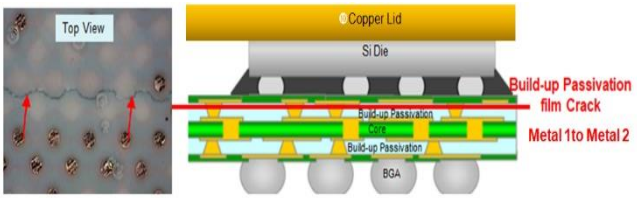

Figure 1: Build-up passivation film crack post temp cycle (TC)

II. Multiphysics Modeling Methodology

A multiphysics scheme was employed to accurately capture the localized stress concentration due to local thermal "hot" spots. Figure 2 below shows the main steps of the methodology. The novelty of the current approach is the inclusion of DIC to accurately capture the localized strain in the region of interest under realistic thermal transient switching conditions. The multiphysics model is then compared to the failure criterion derived from reliability testing.

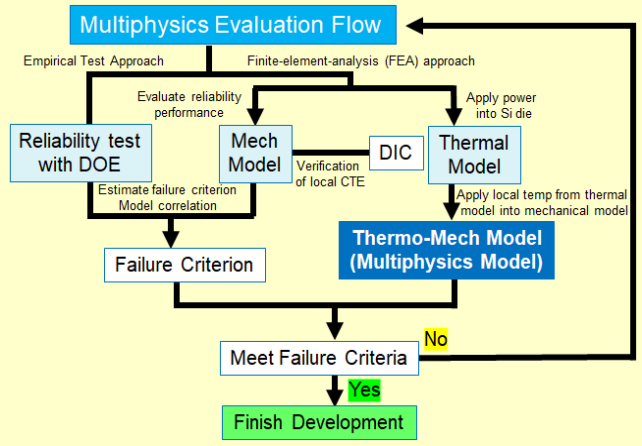

Figure 2: Thermomechanical multiphysics modeling flow.

III. Experimental Procedure of the Calibration Work for the Piezoresistive Stress Sensor

The N-type piezoresistive stress sensors, designed with high precision, exploit the piezoresistive effect-a change in electrical resistivity under mechanical strain. These sensors, manufactured in a (100)-silicon. The design layout is a resistive ladder in an L-shape configuration. One leg is in the <100> direction, and the other is in the <010> direction. The individual legs of the L-shape configuration are Kelvin connected with an external current force input and an external voltage sense output. The connections of the voltage sense output are made close to the piezoresistive sensors to avoid parasitic voltage drop across the metal connections to the sensor components. This design ensures the voltage across the resistor can be measured with high accuracy, enabling highly precise resistance R measurements. Wafer coupons with piezoresistive components were singulated from the wafer material to allow easier handling in the mechanical characterization setups.

To characterize the piezoresistive coefficient of the sensor components, a 4-point bending setup was used to characterize both tensile and compressive stress conditions through extended temperature characterization from -40°C to 125°C. A 4-point bending setup generally consists of two outer supporting and two inner loading pins. The nature of this configuration ensures constant stress conditions between the inner supports without any additional shear forces introduced that could potentially influence the measurements. Inner and outer supports were designed to allow easy movement of the wafer coupons inserted between the supports. The load condition on the supports was either applied by calibrated weights or by a mechanical transducer in a regulation loop with a force sensor.

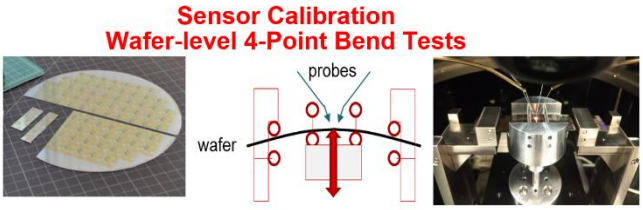

Figure 3: Calibration Work for the Piezoresistive stress sensor with 4 point bend testing on a probe station

The electrical connection to the piezoresistive ladder configuration was made either with wafer probe needles or with wirebond connections. To support simultaneous data collection of multiple piezoresistors, a test-chip was designed to hold the sensor components in a 6x7 array structure with corresponding multiplexers to select individual locations on the die. This test-chip configuration was designed to measure and characterize the package stress conditions arising from packaging and assembly steps.

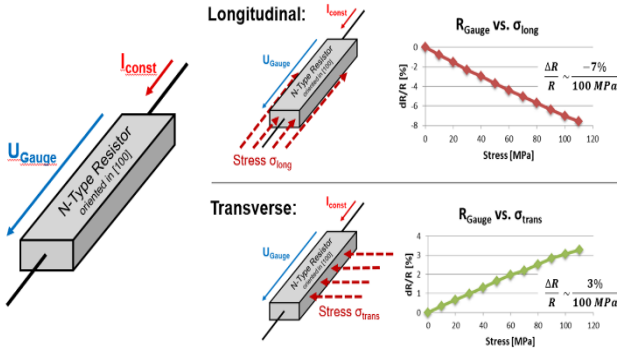

Figure 4: Response of strain gauge to stress longitudinal and transverse to layout orientation

IV. Correlation Work for Stress Magnitude between FEA Based Thermo-Mechanical Model and Stress Sensor

Assessing the exact stress magnitude for semiconductor devices is challenging due to the unexpected residual and intrinsic stresses caused by their complex structure, the bill of material (BOM) set, and process flow. This study installed multiple piezoresistive stress sensors on the Si die to measure the exact stress post-assembly processes and find the critical parameters to minimize the stress gap provided by FEA in the correlation phase. As depicted in figure 5, the chosen package platform type for this correlation work was Quad-Flat-Package (QFP). QFP form factor was chosen to prevent unexpected external stress from being generated during the stress measurement in the socket. This means that the package in the socket during the stress measurement does not receive any external stresses except outer leads to extract the pure stress. The outline of this package and layout of multiple piezoresistive stress sensors are shown in figures 5 and 6. A total of 42 piezoresistive stress sensors with a 6x7 array were installed to understand the stress distribution and trend on the entire Si die.

PKG type	PKG size	Die Size
QFP (64 pin)	10x10mm	4.76x4.94mm (15mil)

Figure 5: Outlines of the package type and details installed piezoresistive stress sensors

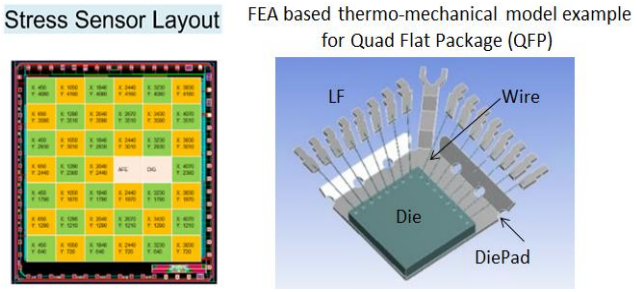

Figure 6: Piezoresistive stress sensor location and details of evaluated package

A. FEA thermo-mechanical model result with elastic properties (Initial Model)

Temperature-dependent isotropic silicon material obeyed the following equations: (1), (2), [4]. A FEA-based thermo-mechanical model was performed to understand the stress magnitude and distribution after assembly processes. A comparison of the stress magnitude and distribution at room temperature (RT) between a piezoresistive stress sensor and FEA result is shown in figure 7. For the stress magnitude, the gap can be seen almost 5x, and the stress distribution trend along the diagonal of the Si-die shows an opposite trend, therefore the FEA-based thermo-mechanical model should be modified with new methodologies to close the gap.

$$C11 = 1.6564\ x\ 102\ x\ exp[-9.4x10^{-5}(T - 298.15)]$$

$$C12 = 0.6394\ x\ 102\ x\ exp[(-9.8x10^{-5}(T - 298.15)]$$

$$C44 = 0.7951\ x\ 102\ x\ exp[(-8.3x10^{-5}(T - 298.15)] \quad (1)$$

$$E[100] = \frac{(C112C12)(C11 - C12)}{C11 + C12}$$

$$E[110] = \left[\frac{C11+C12}{(C11+2C12)(C11-C12)} + \frac{1}{4}\left(\frac{1}{C44} - \frac{2}{C11-C12}\right)\right]^{-1}$$

$$E[111] = \left[\frac{C11+C12}{(C11+2C12)(C11-C12)} + \frac{1}{3}\left(\frac{1}{C44} - \frac{2}{C11-C12}\right)\right]^{-1} \quad (2)$$

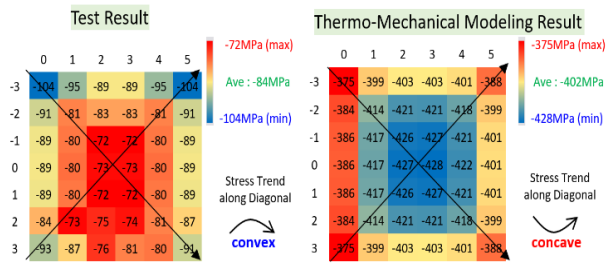

Figure 7: Comparison of stress magnitude and distribution between piezoresistive stress sensor and FEA

B. Material Formulation

The thermomechanical properties of organic material representative of mold compound and substrate materials are sensitive to temperature and strain rate. These are considered to be thermo-rheologically simple viscoelastic materials to reflect a stress relaxation impact at the time domain. The generalized Maxwell model-based viscoelastic behavior was used to input parameters to capture the rate-dependent elastic behavior. The viscoelastic behavior of the generalized Maxwell model kth element can be obtained, and total stress is given by the summation of solutions of (2) up to k=n. The parameters in the equation below are calculated from the dynamic viscoelastic experiment. The experiment is the dynamic response, dynamic mechanical analysis (DMA) with frequency (from 0.1 to 50Hz) /temperature sweep conducted to estimate the rate-dependent elastic properties with the Prony series [5], [6]. Thus a strain is given,

$$\frac{d\varepsilon_k}{dt} = \frac{1}{G_k}\frac{d\sigma_k}{dt} + \frac{\sigma_k}{\eta_k} \tag{1}$$

$$\sigma = \varepsilon_0 G(t) = \varepsilon_0 G_\infty + \varepsilon_0 \sum_{n=1}^{n} G_\infty \exp\left(-t/\tau k\right) \tag{2}$$

$$\varepsilon = \varepsilon_0 e^{i\omega t} \tag{3}$$

After substituting equation (3) into equation (2), the evolution equation for $\sigma(t)$ can be written as,

$$\sigma(t) = \left\{\varepsilon_0 G_\infty + \sum_{n=1}^{n} G_k \varepsilon_0 \frac{i\omega t}{1+\omega^2 {\tau_k}^2}\right\} \exp(i\omega t) \tag{4}$$

$$G'(\omega) = G_\infty + \sum_{n=1}^{n} G_k \frac{\omega^2 {\tau_k}^2}{1+\omega^2 {\tau_k}^2} \tag{5}$$

$$G''(\omega) = \sum_{n=1}^{n} G_k \frac{\omega {\tau_k}^2}{1+\omega^2 {\tau_k}^2} \tag{6}$$

where $G'(\omega)$ is dynamic storage elastic modulus, and $G''(\omega)$ is dynamic loss elastic modulus. Frequency dispersion of specific temperatures is given by using the time-temperature-superposition (TTS) to create the rate-dependent properties at the frequency or time domain from the experimental results of G_∞, G_k, and τ_k by using the least square method. In ANSYS, G_∞ was automatically calculated from other input parameters. Figure 8 presents a practical example of DMA testing for a mold compound with a frequency/temperature sweep test. Figure 9 lists the viscoelastic parameters for the mold compound material with the 20 Prony series. Figure 10 shows the example of a rate-dependent property post-TTS from a master curve derived from DMA data for a mold compound to estimate an appropriate generalized Maxwell model-based viscoelastic parameter with different Prony series (5 and 20). Twenty Prony numbers would be recommended to obtain a smooth master curve [7].

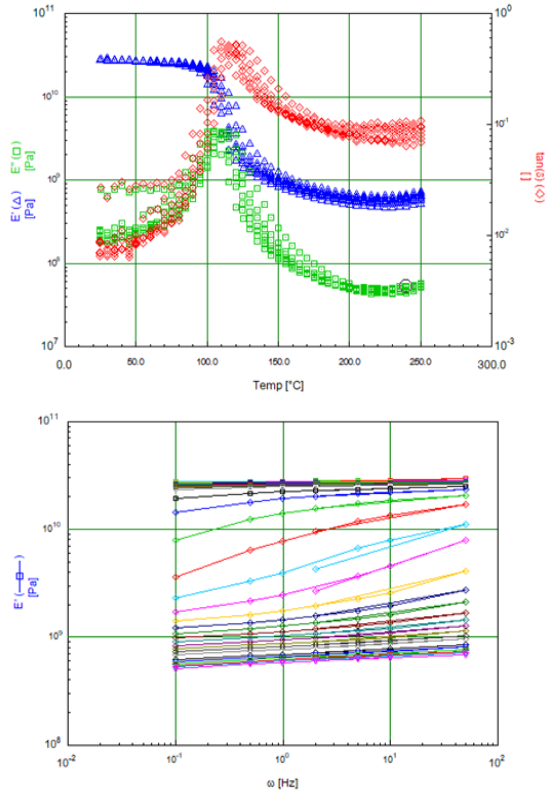

Figure 8: Example of DMA testing for a mold compound with a frequency/temperature sweep test

	k=1	k=2	k=3	k=4	k=5	k=6	k=7	k=8	k=9	k=10
G_k	4.84E-02	1.40E-02	1.08E-02	2.06E-02	2.94E-02	4.77E-02	1.02E-01	1.91E-01	2.34E-01	1.62E-01
τ_k	5.26E-03	5.83E-02	6.46E-01	7.16E+00	7.94E+01	8.80E+02	9.75E+03	1.08E+05	1.20E+06	1.33E+07
	k=11	k=12	k=13	k=14	k=15	k=16	k=17	k=18	k=19	k=20
G_k	6.21E-02	2.60E-02	1.13E-02	8.75E-03	5.78E-03	4.68E-03	3.45E-03	2.30E-03	1.90E-03	2.67E-03
τ_k	1.47E+08	1.63E+09	1.81E+10	2.00E+11	2.22E+12	2.46E+13	2.73E+14	3.02E+15	3.35E+16	3.71E+17

Figure 9: Viscoelastic parameters for the mold compound material with the 20 Prony series at RT (room temperature)

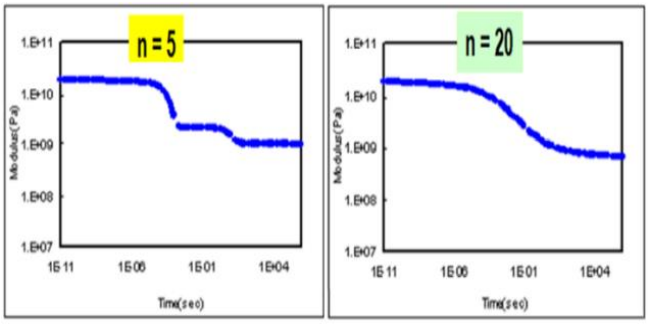

Figure 10: Example of the master curve post-TTS from a DMA data with the different Prony series (5 and 20)

C. Updated FEA thermo-mechanical model result with viscoelastic properties and manufacturing process parameter

An updated FEA-based thermo-mechanical model was performed to close a gap in stress magnitude and distribution compared to the piezoresistive stress sensor. Figure 11 shows the input parameters for the updated models. The generalized Maxwell model-based viscoelasticity to the mold compound and input assembly process parameters in the FEA models helped reflect the rate-dependent behaviors with stress relaxation impact and assembly process-based residual stress. Reference temperatures for the updated FEA-based thermo-mechanical model were the same as those for the mold (including the injection mold and post-mold-cure (PMC) process) and wire-bond (WB) process temperature. Figure 12 shows the stress magnitude and distribution between the piezoresistive stress sensor, initial model, and updated model results. The updated model has an acceptable stress magnitude and distribution compare to the initial model of the piezoresistive stress sensor. From this evaluation, rate-dependent material property and input process parameters, especially mold compound and WB process, are critical to establishing an empirical test correlation of the stress magnitude and distribution.

	Item	Mold	LF/DA/Die Pad
Initial Model	Input property	Elastic	Elastic
	Reference Temp	Mold process temperature	Mold process temperature
Updated Model	Input property	Viscoelastic	Elastic
	Reference Temp	Mold process temperature	WB process temperature

Figure 11: Input process parameters for FEA based thermo-mechanical model

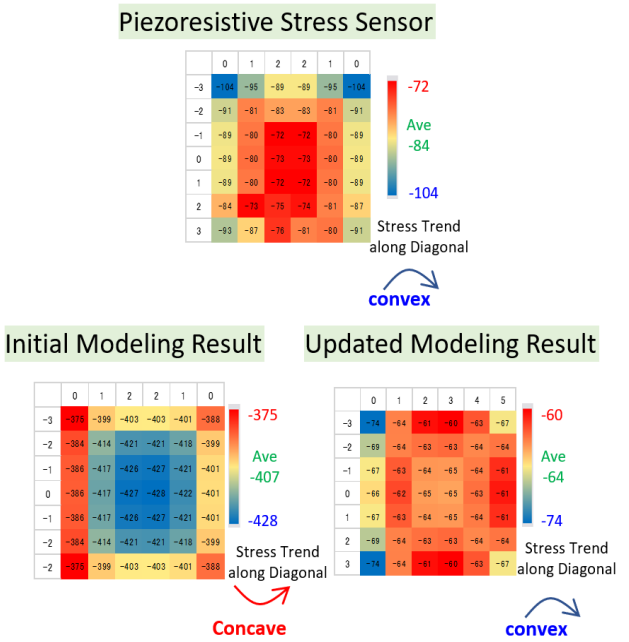

Figure 12: Input process parameters for FEA based thermo-mechanical model

V. Image Processing Technique to Reflect the Local Pattern

A. Material Formulation for the image processing

The mathematical formulation coupled the FEA and DIC homegenization model with CFD thermal analysis. Using the following equation, the homogenization model was adopted to reflect the regional copper trace in the substrate for the FC devices [1].

$$E_s = \emptyset_{cu}E_{cu} + (1-\emptyset_{cu})E_{BP}, \alpha s = \emptyset_{cu}E_{BP} + (1-\emptyset_{cu})\alpha_{BP} \quad (7)$$

where φ is the volume fraction, E is Young's modulus, α is the CTE. An image processing technique was utilized to reflect the local metal layers in the substrate into the FEA-based thermo-mechanical simulations and help prevent the compression of FEA-based thermo-mechanical model sizes. First, the original substrate drawing should be translated to the gray scale-based 8-bit color image files with appropriate image resolution utilizing an image processing technique called light-intensity analysis (LIA) to reflect the local metal patterns into the FEA-based mechanical models. Light intensity values of 0 and 255 represent complete black and white colors, which means 0% and 100% local metal regions, respectively. After LIA, the homogenization material model was utilized to reflect the regional metal fraction in the substrate using the following equation [1] for the FEA-based thermo-mechanical simulation. This image processing technique is also utilized for the correlation/verification work with the digital image correlation (DIC). Figure 13 shows an example of a post-

image processing technique with the light intensity values utilizing LIA for the part of the substrate. The homogenization material should be assigned based on the light intensity value to reflect the local metal density in the substrate.

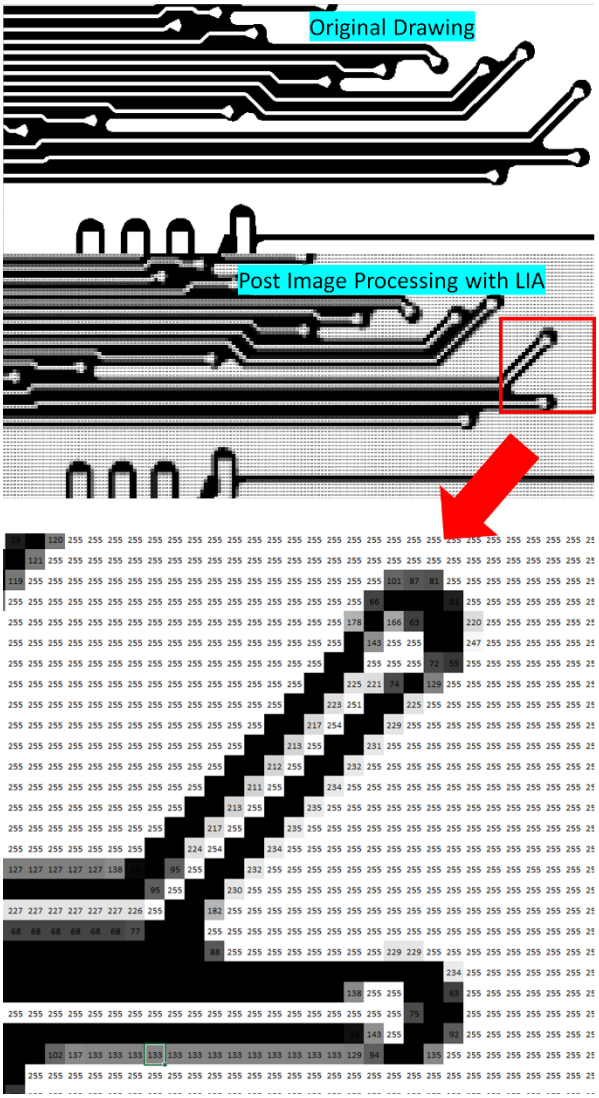

Figure 13: Example of the image processing technique for the local metal pattern in the substrate

B. Digital Image Correlation (DIC)

The principle of DIC to estimate the thermal strain in the local region is shown in figure 14. Binocular vision is installed in the DIC tool to extract the x-y plane coordinate and the z directional coordinate, which can compute the thermal strain in the x-y plane. As for DIC characterization, a specific pattern, called speckle-pattern should be created on the specimen's surface first, and its speckle surface should be divided into microscopic areas called subsets. Subsequently, DIC estimates the local thermal strain in-plane by extracting the local displacement change of a subset image on the specimens with a visual approach using high-magnification optical lenses [2].

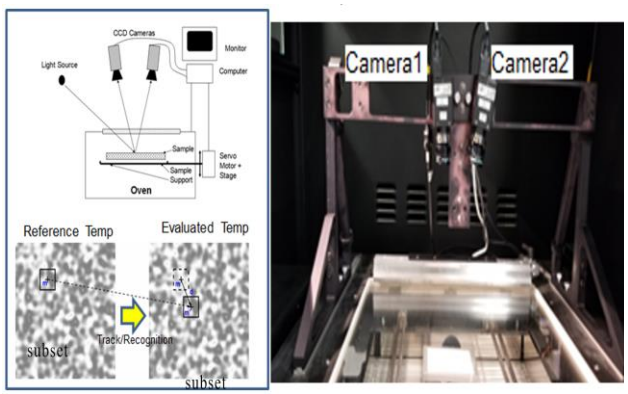

Figure 14: Digital image correlation characterization approach.

DIC characterization accuracy highly depends on the speckle patterns. Three kinds of speckle patterns were evaluated to understand the pattern impact. Figure 15 shows the noise analysis between three types of speckle patterns; larger speckle patterns are prone to generate colossal noise. Figure 16 shows the substrate CTE contour map and temperature-dependent CTE with TMA and DIC as a verification. The distribution of CTE trend for the substrate between the DIC and FEA-based thermomechanical models is similar. For the material verification, the substrate CTE contour map and the substrate temperature-dependent CTE with TMA and DIC are shown in figure 17.

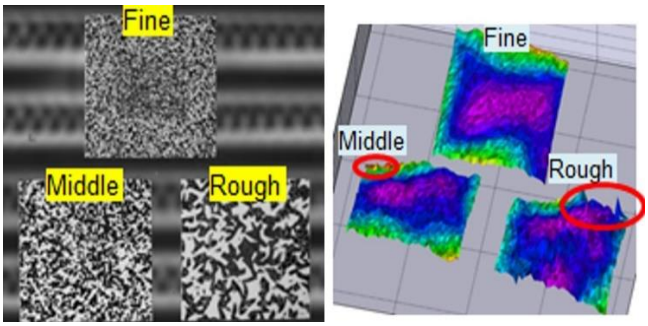

Figure 15: Example of speckle patterns and noise analysis.

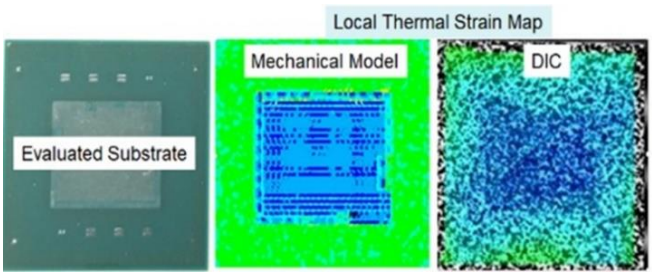

Figure 16: CTE map of the substrate (thermo-mechanical model and DIC)

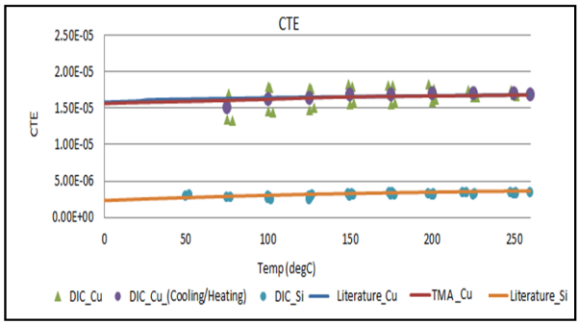

Figure 17: Material verification of coefficient of thermal expansion (CTE) with DIC.

VI. Multiphysics Modeling Approach

A. Mechanical Modeling approach

The outline of the FC device is shown in figure 18. The empirical test correlation utilizing the coupling of the FEA-based thermo-mechanical and test results was established to estimate the build-up of the passivation crack risk. Details of test vehicles and mechanical properties are listed in figure 19. As for test vehicle (TV) 2, a build-up passivation crack was observed post-TC loading (temperature range: -55° C /150°C). As a result, this test vehicle was used as a failure criterion.

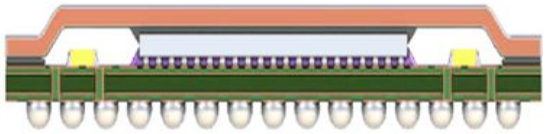

PKG type	PKG size	Die Size
Lidded FC ball-grid-array (FC-BGA)	23x23 mm	12.8x11.3mm

Figure 18: Outlines of the package type and details installed piezoresistive stress sensors

DOE	Underfill		Substrate Core	
TV1	Sample A		Sample A	
TV2	Sample A		Sample B	
TV3	Sample B		Sample A	
TV4	Sample B		Sample B	
	Underfill		Substrate Core	
	Modulus (GPa)	CTE (ppm/C)	Modulus (GPa)	CTE (ppm/C)
Sample A	Reference			
Sample B	0.85 x	1.15 x	1.10 x	1.15x

Figure 19: Evaluated DOE and mechanical properties.

Copper pillar bump with solder was used as a first level interconnection between Si die and the substrate. For lead-free solder, rate-dependent plasticity, known as the Anand model based on the improvement of the Garofalo model, was characterized [7]. This model has been widely used in the semiconductor industry to capture the rate-dependent plasticity of solder material under the reliability test. Material constraints of Anand's viscoplastic constitutive model can be fitted to the strain rate and steady-state stress tests based on equations (8) and (9), and related strain hardening material parameters can be fitted based on (10) and (11) data based on stated equations. To estimate the remaining Anand's parameters, all the stress-strain data from the characterization is used to fit the following stress-strain relationship (12), [8]. Figure 20 lists Anand's viscoplastic parameters of solder material for the evaluated FC device as a 1st level interconnection.

$$\frac{d\varepsilon^p}{dt} = A \exp\left(-\frac{Q}{RT}\right)\left[\sinh\left(\frac{\zeta\sigma}{s}\right)\right]^{1/m} \tag{8}$$

$$\sigma^* = \frac{\hat{s}}{\zeta}\left\{\frac{1}{A}\frac{d\varepsilon^p}{dt}\exp\left(\frac{Q}{RT}\right)\right\}^n * \sinh^{-1}\left[\left\{\frac{1}{A}\frac{d\varepsilon^p}{dt}\exp\left(\frac{Q}{RT}\right)\right\}^m\right] \tag{9}$$

$$\frac{d\sigma}{d\varepsilon^p} = ch_0\left(1-\frac{\sigma}{\sigma^*}\right)^a, \qquad \sigma = cs \ , \ \sigma^* = cs^* \tag{10}$$

$$c \equiv \frac{1}{\zeta}\sinh^{-1}\left[\left\{\frac{1}{A}\frac{d\varepsilon^p}{dt}\exp\left(\frac{Q}{RT}\right)\right\}^m\right] \tag{11}$$

$$\sigma = \sigma^* - [(\sigma^* - cs_0)^{(1-a)} + (a-1)\{(ch_0)(\sigma^*)^{-a}\}\varepsilon_p]^{1/(1-a)} \tag{12}$$

Initial Deformation Resistance	s_0 (MPa)	2.15E+00
Activation energy/Boltzmann's constant	Q/R (/K)	9.97E+03
Pre-exponential factor	A (s^{-1})	1.80E+01
Multiplier of stress	ξ	3.50E-01
Strain rate sensitivity of stress	m	1.53E-01
hardening/softening constant	h_0(MPa)	1.53E+03
coefficient for deformation resistance saturation	$\hat{S}$ (MPa)	2.54E+00
strain rate sensitivity of saturation	n	2.80E-02
strain rate sensitivity of hardening or softening	a	1.69E+00

Figure 20: ANAND viscoplastic parameters of solder material for FC bump.

Figure 21 shows the example of thermo-mechanical model of lidded FC-BGA device. Reflecting the geometric details of the global and local level modeling technique were performed. Figure 22 shows the actual failure location of the build-up passivation cracks post-TC loading based on failure analysis and elastic strain-energy-density contour map by thermo-mechanical modeling result. The failure location of the build-up passivation cracks and failure trend were close to thermo-mechanical modeling results.

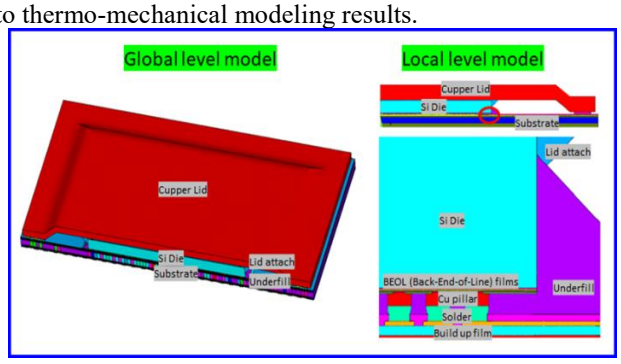

Figure 21: Example of thermo-mechanical model for lidded FC-BGA device

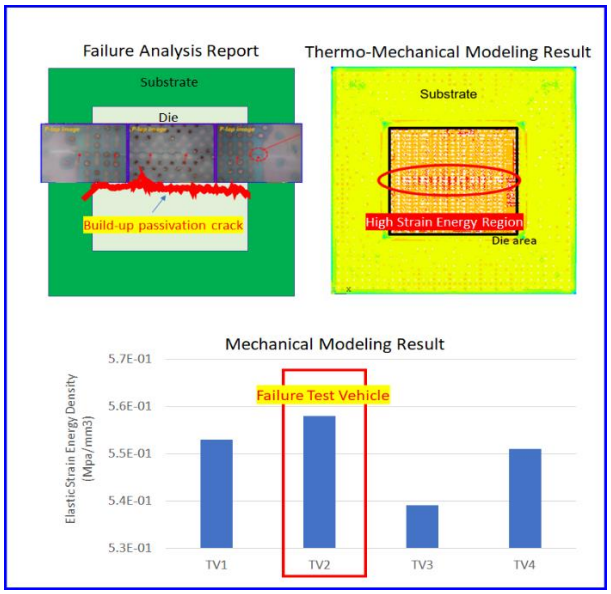

Figure 22: Stress contour map by thermo-mechanical modeling result and the strain energy comparison

B. Thermal modeling approach

The governing equation of the thermal analysis is based on conservation of energy and can be written as:

$$\rho c_p \frac{\partial T}{\partial t} = \nabla (\kappa \nabla T) + q \qquad (13)$$

where ρ is the mass density, c_p is the specific heat capacity, κ is the thermal conductivity, T represents the temperature, and q denotes the rate of volumetric heat generation. Thermal simulations can be used both to characterize the thermal performance and quantify the temperature gradient across a semiconductor device under specific conditions. Depending on the design and construction of the silicon die and the package substrate, temperature gradients can induce more significant stress concentrations than would be otherwise predicted by thermo-mechanical modeling. That is assuming uniform temperatures within a body. The most significant temperature gradients can be introduced by high-power dissipation pulses for short time durations, for example, during the initial startup phases for the device operation. These conditions produce copious amounts of heat on the silicon die while not allowing time for the heat to spread within the package. From the package, it is mounted on to effectively dissipate the heat. To utilize the multiphysics modeling approach, a thermal simulation was run using CFD software. This simulation assumed 103.8 watts of power dissipation lasting 0.25 seconds on the die. The power dissipation was concentrated on certain areas of the die ("hot spots") based on the silicon design. These hot spot areas increase the temperature gradients across the die because the power dissipation and heat flux is larger in certain areas than in others. The results of the CFD simulation are shown in figure 23.

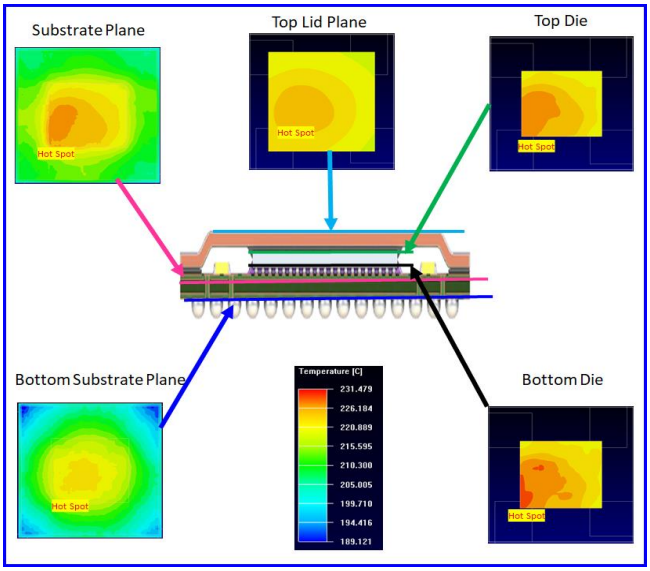

Figure 23: Temperature gradient map regarding the surface of the die, lid, a3d substrate at end of 0.25 second thermal simulation.

C. Multiphysics modeling approach

The high-power dissipation pulses for short durations, which generated substantial thermal stress should be optimized. Optimization is needed to ensure the strain energy density would not exceed the criterion based on the empirical test correlation at the design stage – that is, as determined by the multiphysics modeling. The multiphysics modeling approach evaluated the three kinds of build-up materials to mitigate the build-up film crack risk. Figure 24 lists the mechanical properties and viscoelastic parameters for these

three build-up passivation film materials with the 20 Prony series. Figure 25 shows the multiphysics modeling result. Multiphysics modeling results reflecting the hot spot show a higher strain-energy-density magnitude than the mechanical reliability under the TC test. As a comparison between these three build-up materials, the build-up C would show the lowest strain-energy density and is lower than the criterion based on the empirical test correlation. Since this critical stress intensity factor (KIc) for this build up material shows the highest value, build-up C is expected to mitigate this crack risk.

	Young's Modulus (GPa)	CTE (ppm/C)	Critical stress intensity factor K_{IC} (MPa*m$^{1/2}$)
Build-up A	Reference		
Build-up B	1.6 x	0.6 x	1.1x
Build-up C	2.1 x	0.5 x	1.5x

			k=1	k=2	k=3	k=4	k=5	k=6	k=7	k=8	k=9	k=10
Build-up A	25C	G_k	6.64E-02	2.36E-02	2.46E-02	0.00E+00	0.00E+00	3.96E-02	4.43E-02	6.94E-02	7.62E-02	6.94E-02
		τ_k	7.96E-03	1.26E-01	2.00E+00	3.18E+01	5.05E+02	8.01E+03	1.27E+05	2.02E+06	3.20E+07	5.07E+08
	125C	G_k	6.37E-02	2.33E-02	2.61E-02	2.60E-02	4.55E-02	0.00E+00	4.37E-02	5.74E-02	1.93E-02	9.81E-02
		τ_k	1.17E-11	2.26E-10	4.39E-09	8.52E-08	1.65E-06	3.21E-05	6.22E-04	1.21E-02	2.34E-01	4.55E+00
	250C	G_k	6.67E-02	2.43E-02	2.69E-02	2.69E-02	4.76E-02	0.00E+00	4.23E-02	5.16E-02	2.93E-02	8.19E-02
		τ_k	6.93E-26	1.28E-24	2.35E-23	4.33E-22	7.97E-21	1.47E-19	2.70E-18	4.98E-17	9.17E-16	1.69E-14
Build-up B	25C	G_k	6.71E-02	2.16E-02	2.28E-02	3.29E-02	3.28E-02	3.41E-02	4.44E-02	4.39E-02	5.06E-02	6.14E-02
		τ_k	7.96E-03	9.52E-02	1.14E+00	1.36E+01	1.63E+02	1.95E+03	2.33E+04	2.79E+05	3.33E+06	3.99E+07
	125C	G_k	5.88E-02	2.40E-02	2.30E-02	2.96E-02	3.18E-02	3.13E-02	3.54E-02	3.73E-02	4.76E-02	4.81E-02
		τ_k	4.78E-11	6.98E-10	1.02E-08	1.49E-07	2.17E-06	3.17E-05	4.63E-04	6.77E-03	9.88E-02	1.44E+00
	250C	G_k	5.94E-02	2.43E-02	2.29E-02	2.98E-02	3.17E-02	3.22E-02	3.50E-02	3.70E-02	4.82E-02	4.72E-02
		τ_k	1.28E-23	1.81E-22	2.56E-21	3.62E-20	5.12E-19	7.25E-18	1.03E-16	1.45E-15	2.05E-14	2.90E-13
Build-up C	25C	G_k	6.73E-02	2.49E-02	2.30E-02	2.58E-02	3.43E-02	4.25E-02	5.30E-02	6.18E-02	7.78E-02	9.61E-02
		τ_k	7.96E-03	1.14E-01	1.63E+00	2.33E+01	3.33E+02	4.76E+03	6.80E+04	9.72E+05	1.39E+07	1.99E+08
	125C	G_k	6.37E-02	2.69E-02	2.73E-02	2.75E-02	2.34E-02	3.31E-02	4.02E-02	5.73E-02	7.46E-02	9.97E-02
		τ_k	2.43E-11	3.62E-10	5.40E-09	8.06E-08	1.20E-06	1.80E-05	2.68E-04	4.00E-03	5.97E-02	8.91E-01
	250C	G_k	6.39E-02	2.72E-02	2.58E-02	2.97E-02	2.10E-02	3.04E-02	3.76E-02	5.36E-02	6.74E-02	9.92E-02
		τ_k	2.48E-23	3.33E-22	4.47E-21	5.99E-20	8.03E-19	1.08E-17	1.44E-16	1.94E-15	2.60E-14	3.49E-13

			k=11	k=12	k=13	k=14	k=15	k=16	k=17	k=18	k=19	k=20
Build-up A	25C	G_k	8.40E-02	1.12E-01	1.42E-01	1.10E-01	6.23E-02	3.48E-02	1.77E-02	7.67E-03	2.97E-03	1.80E-03
		τ_k	8.05E+09	1.28E+11	2.03E+12	3.22E+13	5.10E+14	8.09E+15	1.28E+17	2.04E+18	3.23E+19	5.13E+20
	125C	G_k	7.55E-02	1.03E-01	1.18E-01	1.57E-01	1.09E-01	1.87E-02	3.51E-03	0.00E+00	4.23E-04	7.70E-04
		τ_k	8.82E+01	1.71E+03	3.32E+04	6.44E+05	1.25E+07	2.42E+08	4.70E+09	9.13E+10	1.77E+12	3.44E+13
	250C	G_k	9.09E-02	1.31E-01	2.01E-01	1.30E-01	3.02E-02	4.78E-03	2.10E-03	4.37E-05	4.82E-04	8.00E-04
		τ_k	3.11E-13	5.72E-12	1.05E-10	1.94E-09	3.57E-08	6.58E-07	1.21E-05	2.23E-04	4.11E-03	7.57E-02
Build-up B	25C	G_k	8.32E-02	1.06E-01	1.30E-01	1.34E-01	7.50E-02	2.02E-02	4.94E-03	2.97E-03	2.11E-03	2.59E-03
		τ_k	4.77E+08	5.70E+09	6.82E+10	8.15E+11	9.75E+12	1.17E+14	1.39E+15	1.67E+16	1.99E+17	2.39E+18
	125C	G_k	6.95E-02	9.56E-02	1.23E-01	1.51E-01	1.14E-01	3.85E-02	7.33E-03	3.42E-03	2.26E-03	2.63E-03
		τ_k	2.11E+01	3.07E+02	4.49E+03	6.55E+04	9.57E+05	1.40E+07	2.04E+08	2.98E+09	4.35E+10	6.35E+11
	250C	G_k	6.46E-02	9.77E-02	1.48E-01	1.64E-01	8.95E-02	2.70E-02	7.09E-03	3.37E-03	2.27E-03	2.65E-03
		τ_k	4.11E-12	5.81E-11	8.22E-10	1.16E-08	1.65E-07	2.33E-06	3.29E-05	4.66E-04	6.59E-03	9.33E-02
Build-up C	25C	G_k	1.13E-01	1.20E-01	1.01E-01	6.32E-02	3.50E-02	1.80E-02	9.08E-03	5.57E-03	3.86E-03	3.76E-03
		τ_k	2.84E+09	4.06E+10	5.81E+11	8.30E+12	1.19E+14	1.70E+15	2.43E+16	3.47E+17	4.96E+18	7.09E+19
	125C	G_k	1.19E-01	1.28E-01	1.09E-01	6.95E-02	3.76E-02	1.94E-02	9.63E-03	5.74E-03	3.96E-03	3.81E-03
		τ_k	1.33E+01	1.98E+02	2.96E+03	4.42E+04	6.60E+05	9.85E+06	1.47E+08	2.19E+09	3.27E+10	4.88E+11
	250C	G_k	1.24E-01	1.41E-01	1.14E-01	6.93E-02	3.48E-02	1.73E-02	9.35E-03	5.82E-03	3.85E-03	3.85E-03
		τ_k	4.67E-12	6.27E-11	8.41E-10	1.13E-08	1.51E-07	2.03E-06	2.72E-05	3.65E-04	4.89E-03	6.56E-02

Figure 24: Mechanical properties and viscoelastic parameters for the build-up passivation films material

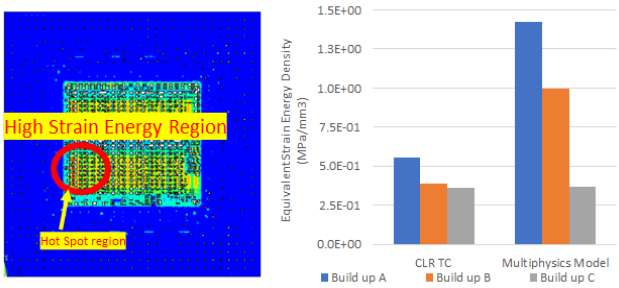

Figure 25: Multiphysics modeling results showing impact of coupled thermomechanical modeling.

VII. Conclusion

Multiple piezoresistive stress sensors were used to correlate the stress magnitude and distribution of Si-die installed in a semiconductor package compared to FEA-based thermo-mechanical models. Critical findings for achieving good correlations of stress distribution and magnitude between the multiphysics simulation flow results and measured data are utilizing rate-dependent properties and reflecting manufacturing process parameters. DIC and image processing-based LIA were performed for the material verification phase to reflect the local metal density in the substrate into the thermo-mechanical model. In addition, a multiphysics modeling approach was developed to reflect that the temperature gradients have the potential to induce more significant stress concentrations based on the thermal simulation, which cannot be captured by using the typical conventional methodology. Therefore, the compilation of these methodologies used in tandem can be utilized to mitigate unexpected failure risks for future devices at the design stage.

Acknowledgment

The authors gratefully acknowledge the support of Texas Instruments' Semiconductor Packaging Department, ATD, and Freising for funding and providing resources for this evaluation and data collection.

References

[1] U. W. Suter and B. E. Eichinger, "Estimating elastic constants by averaging over simulated structures," Polymer, vol. 43, 2002.

[2] Po Yu Liad "Die Bonding Solution for Flip Chip-Chip Schale Package- DIC (Digital Image Correlation) and Shadow Moire Application "2022 IEEE 72nd Electronic Components and Technology Conference (ECTC).

[3] Yutaka Suzuki, Jaimal Williamson, Blake Travis, Rajen Murugan, "Multiphysics Reliability Modeling of Flip Chip (FC) Package Build Up Film Passivation Crack", 2023 IEEE MTT-S International Conference on Numerical Electromagnetic and Multiphysics Modeling and Optimization (NEMO'2023), Winnipeg, MB, Canada, June 28 - 30, 2023.

[4] INSPEC, Properties of silicon EMIS Datareiews Series No.4, 14 (1988)

[5] B.V. Milosheva; K.M.B. Jansen; J.H.J. Janssen; H.J.L. Bressers; L.J. Ernst, "Viscoelastic characterization of fast curing moulding compounds" EuroSimE 2005. Proceedings of the 6th International Conference on Thermal, Mechanial and Multi-Physics Simulation and Experiments in Micro-Electronics and Micro-Systems, 2005.

[6] Yutaka Suzuki, Masazumi Amagai "A study of material properties for package flatness in 3D package" 2008 IEEE 9th VLSI

[7] L. Anand, "Constitutive equations for hot-working metals," International Journal of Plasticity, Volume 1, Issue 3, 1985

[8] Jaimal Williamson, Yutaka Suzuki, and Ron Eller "Impact of FCBGA substrate stack-up on BLR performance" IMAPS 2022 - 55th International Symposium on Microelectronics